Tunneling exit characteristics from classical backpropagation of an ionized electron wave packet

Hongcheng Ni, Ulf Saalmann, and Jan-Michael Rost

Max-Planck-Institut für Physik komplexer Systeme, Nöthnitzer Straße 38, 01187 Dresden, Germany

We investigate tunneling ionization of a single active electron with a strong and short laser pulse, circularly polarized. With the recently proposed backpropagation method, we can compare different criteria for the tunnel exit as well as popular approximations in strong-field physics on the same footing. Thereby, we trace back discrepancies in the literature regarding the tunneling time to inconsistent tunneling exit criteria. The main source of error is the use of a static ionization potential, which is, however, time dependent for a short laser pulse. A vanishing velocity in the instantaneous field direction as tunneling exit criterion offers a consistent alternative, since it does not require the knowledge of the instantaneous binding energy. Finally, we propose a mapping technique that links observables from attoclock experiments to the intrinsic tunneling exit time.

I. INTRODUCTION

Tunneling phenomena have given rise to controversies almost since the birth of quantum mechanics. In particular, the question of how much time it takes to tunnel has been debated frequently [1–3], most recently in the context of strong-field tunneling ionization [4–6]. This type of electron tunneling is triggered by a laser pulse, whose electric field is comparable to the Coulomb field bound electrons experience from the nucleus. This strong electric field bends down the Coulomb potential periodically in one direction and results in a barrier. If the top of the barrier is below the initial energy of the bound electron, one speaks of "over-the-barrier" ionization, which is classically allowed. In the opposite situation, however, the electron can only escape quantum mechanically by tunneling. Since the probability of this process depends exponentially on the barrier and therefore on the electric field strength of the laser, the latter suggests itself as a trigger for tunneling ionization, starting a clock to measure the time that elapses before the electron has tunneled out. If one uses a short, elliptically polarized infrared laser pulse, the angle at which the ionized electron appears at the detector can be compared to the direction of the maximal laser electric field and from a possible difference a time delay can be inferred using the angular frequency of the light. This is the principle of the attoclock [7,8].

The idea to "measure" possible tunneling ionization times directly in this setup is very appealing. Yet, it actually adds to the notoriously difficult problem of tunneling through *static* barriers the difficulty of nonadiabaticity: Since the barrier is now time-dependent, the tunneling electron may gain or lose energy. Moreover, the electron is asymptotically not free but subject to the long-range attraction of the ionic core, which, by itself, generates a time delay. Although substantial obstacles, these difficulties are technical and can be overcome (as we will see). What remains is the fundamental question how to define tunneling in the first place such that it can be clocked, not to speak of a possible measurement.

While we do not have a definite answer, we have proposed to define tunneling by classically forbidden dynamics, i.e., by propagating classical trajectories. We have shown [9]

that classical backpropagation of a wave packet, quantum-mechanically ionized in a strong circularly polarized laser pulse, can provide a consistent definition of tunneling and the time it takes. In addition, we were able to formulate a criterion that reveals if the ionization process has tunneling character in the first place. Finally, our classical backpropagation allows us to compare different tunneling criteria that have been proposed on the same footing, in particular criteria based on spatial and momentum conditions for the tunnel exit. Thereby, we will be able to clarify the origin of contradicting published results [9–17], which have been difficult to contrast with each other so far since they use different approximations to the entire electron dynamics along with a respectively different tunneling criterion. We can easily examine the effect of these different tunneling criteria using the same dynamics, namely our classical backpropagation.

Before we do so, we present in Sec. II a detailed account of the classical backpropagation as introduced in Ref. [9]. In Sec. III, we extract the tunneling coordinates with the velocity criterion and analyze their intensity dependence. In Sec. IV, we proceed analogously with the position criterion to define tunneling ionization and demonstrate that this leads to inconsistent results. The section includes a reanalysis of a recent theoretical [15] and experimental [16] study with the velocity criterion, demonstrating that in both cases zero tunneling time results. In Sec. V, we describe a mapping technique to link the tunneling exit time to experimental observables. Conclusions are given in Sec. VI.

II. BACKPROPAGATION AND IDENTIFICATION OF TUNNELING

The essence of classical backpropagation is to first quantum-mechanically propagate the initial state forward to some time after the laser pulse has ended which avoids any assumptions or approximations. In a second step the ionized part of the propagated wave packet is extracted and transcribed to classical phase space with the help of the local-momentum method [18,19]. In the third step the wave packet is backprop-
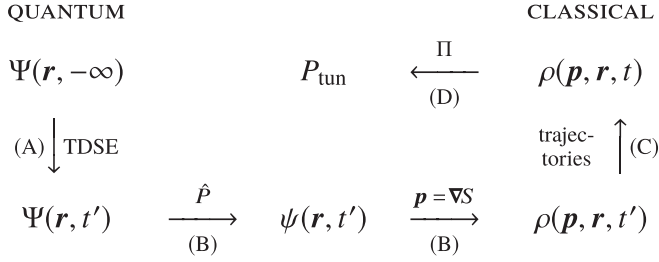
QUANTUM   CLASSICAL

$\Psi(\boldsymbol{r}, -\infty)$ P_{tun} $\xleftarrow[\text{(D)}]{\Pi}$ $\rho(\boldsymbol{p}, \boldsymbol{r}, t)$

(A) $\bigg\downarrow$ TDSE   trajec- $\bigg\uparrow$ (C)
                                             tories

$\Psi(\boldsymbol{r}, t')$ $\xrightarrow[\text{(B)}]{\hat{P}}$ $\psi(\boldsymbol{r}, t')$ $\xrightarrow[\text{(B)}]{\boldsymbol{p}=\nabla S}$ $\rho(\boldsymbol{p}, \boldsymbol{r}, t')$

FIG. 1. Schematic overview of the classical backpropagation method to extract tunneling parameters: (A) quantum forward propagation of an initial state $\Psi(\boldsymbol{r})$ until time t' (Sec. II A), (B) extraction of ionized part of the wave packet and transcription to a classical phase-space density $\rho(\boldsymbol{p}, \boldsymbol{r}, t')$ (Sec. II B), (C) classical backpropagation (Sec. II C), and (D) extraction of tunneling exit distributions (Sec. II D).

agated with classical trajectories and finally, tunneling exit properties are extracted with suitable projectors corresponding to the specific tunneling criterion applied. These steps are schematically summarized in Fig. 1.

Note that the idea of propagating the wave packet backward in time itself is not new but has been applied in many areas. Probably most fundamental is the S-matrix for collisions, a product of two Møller operators $\Omega^{(\pm)}$ [20]. First, with $\Omega^{(-)}$ the projectile and target are propagated backwards without interaction, and then forward with interaction. In a second step the same is done in the forward direction to connect with the respective asymptotic states. Such forward–backward propagation with slightly different Hamiltonians has been termed quantum fidelity [21] in the context of error assessment for quantum computing and has also gained popularity in semiclassics [22,23]. Backpropagation is also used in quantum optimal control to obtain the best electric field for a certain optimization goal [24,25]. In the present context of intense-field interactions the backpropagation has been used to obtain the Wigner–Smith time delay [26,27] in photoemission [28,29].

While in all these examples, forward and backward propagation were formulated quantum mechanically, we rely on *classical* backpropagation as an essential element to identify the tunneling dynamics. This unusual combination of a quantum forward and a classical backpropagation brings about new possibilities of extracting classical features from quantum processes without approximating the accurate quantum dynamical evolution. In the present study, in particular, this concept provides the first means to retrieve the tunneling exit time without approximating the ionization dynamics to obtain a tunneling scenario, which is a prerequisite to define the tunneling exit time.

A. Quantum forward propagation

We will focus on a realization of tunneling ionization by a short circularly polarized pulse for a single active electron (SAE) model of helium in two spatial dimensions. This problem is of sufficient complexity to contain all features of tunneling ionization, yet it is simple enough to facilitate its computation and its interpretation in terms of visualization of distributions. We use the split-step Fourier method (or Fourier grid method) to numerically solve the time-dependent

Schrödinger equation (TDSE) for the model helium atom with the SAE potential $V(\boldsymbol{r})$ [30] on a grid in space (two-dimensional) and time (atomic units are used unless stated otherwise),

$$i\frac{\partial}{\partial t}\Psi(\boldsymbol{r}, t) = \left\{\frac{1}{2}[\boldsymbol{p} + \boldsymbol{A}(t)]^2 + V(\boldsymbol{r})\right\}\Psi(\boldsymbol{r}, t), \quad \text{(1a)}$$

where $\boldsymbol{p}$ is the momentum operator and

$$\boldsymbol{A}(t) \equiv \begin{pmatrix} A_x(t) \\ A_y(t) \end{pmatrix} = \frac{A_0 \cos^4[\omega t/(2N)]}{\sqrt{\epsilon^2 + 1}} \begin{pmatrix} \cos(\omega t) \\ \epsilon \sin(\omega t) \end{pmatrix} \quad \text{(1b)}$$

is the vector potential of the laser field, with peak value A_0, ellipticity ϵ, angular frequency ω, and a duration of N optical cycles. The corresponding electric field is obtained from $\boldsymbol{F}(t) = -\frac{d}{dt}\boldsymbol{A}(t)$. Note that $t = 0$ corresponds to the pulse center and $\boldsymbol{A}(t) = 0$ unless $|t| < N\pi/\omega$.

The TDSE is solved as before [9], starting with the ground state of $V(\boldsymbol{r})$. For the laser pulse, we use a two-cycle ($N = 2$) circularly polarized ($\epsilon = 1$) infrared laser pulse with angular frequency $\omega = 0.045$.[1] For testing numerical accuracy, the TDSE has been solved in both length and velocity gauge, whereby identical final results were produced.

B. From the quantum wave function to the classical phase-space distribution

From the propagated state $\Psi(\boldsymbol{r}, t')$ at a time t' when the laser pulse is over, the ionized wave packet $\psi(\boldsymbol{r}, t')$ is obtained by discarding in the wave function a sphere of radius r_c, in which only the remaining bound-state amplitude is assumed to be localized,

$$\psi(\boldsymbol{r}, t') = \Theta(r - r_c)\Psi(\boldsymbol{r}, t'). \quad \text{(2)}$$

Using $r_c = 12$ a.u., we have verified that the resulting ionized wave packet produces the same results as a wave packet $\psi(\boldsymbol{r}, t')$ obtained by projecting out the lowest 16 bound eigenstates from the final state $\Psi(\boldsymbol{r}, t')$.

The ionized wave packet $\psi(\boldsymbol{r}, t')$ can now be regarded as the "initial condition" to initiate the backpropagation. To this end, we write the quantum ionized wave packet $\psi(\boldsymbol{r}, t') \equiv R(\boldsymbol{r}, t')\exp[i S(\boldsymbol{r}, t')]$ in terms of real amplitude and phase and transcribe it to a classical phase-space distribution using the local-momentum [18,19]. Defining

$$\boldsymbol{p}(\boldsymbol{r}) = \nabla S(\boldsymbol{r}), \quad \text{(3a)}$$

we get

$$\rho(\boldsymbol{p}, \boldsymbol{r}, t') = R^2(\boldsymbol{r}, t')\,\delta(\boldsymbol{p} - \nabla S(\boldsymbol{r}, t')), \quad \text{(3b)}$$

for the phase-space distribution representing the quantum ionized wave packet.

In Fig. 2 we compare the momentum distribution of the ionized electron from the model helium atom obtained by the

---

[1]For a short finite laser pulse, the electric field has a different frequency than the vector potential. For our laser parameters here, this corresponds to $\omega_F = 0.057$ for the electric field, or 800 nm wavelength. The physical observables, on the other hand, are more closely related to the frequency of the vector potential.
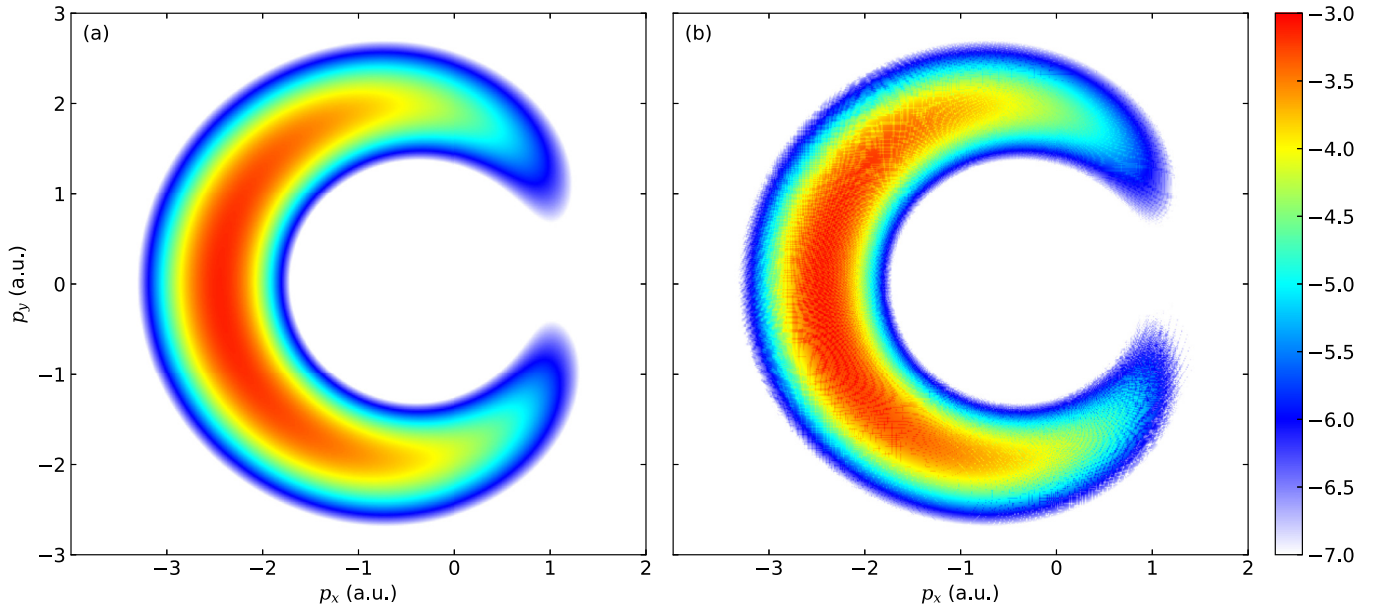
FIG. 2. Momentum distribution of the ionized electron after the laser pulse at time t' for the model helium atom generated from the ground state (in logarithmic scale) with a circularly polarized laser pulse [Eq. (1b)] of two optical cycles length, an angular frequency $\omega = 0.045$, and a peak intensity of 8×10^{14} W/cm^2. The momentum distributions are obtained (a) as $|\widetilde{\psi}(\boldsymbol{p}, t')|^2$ from the Fourier transform of the ionized wave function $\psi(\boldsymbol{r}, t')$ [Eq. (2)] and (b) as $\rho(\boldsymbol{p}, t')$ from the local-momentum method, see Eq. (4b).

local-momentum to its quantum counterpart $\widetilde{\psi}(\boldsymbol{p}, t')$ obtained from $\psi(\boldsymbol{r}, t')$ by Fourier transform. Clearly, both distributions are quite similar, which is confirmed by the overlap of the densities,

$$\frac{\int d^2 p \, |\widetilde{\psi}(\boldsymbol{p}, t')| \sqrt{\rho(\boldsymbol{p}, t')}}{\int d^2 p \, |\widetilde{\psi}(\boldsymbol{p}, t')|^2} = 0.998, \qquad (4a)$$

close to one, where

$$\rho(\boldsymbol{p}, t') = \int d^2 r \, \rho(\boldsymbol{p}, \boldsymbol{r}, t'). \qquad (4b)$$

Note that via its construction with the local-momentum method, ρ in Eq. (3b) is essentially a two-dimensional distribution and not a full four-dimensional one. It can be rigorously derived in the limit $\hbar \rightarrow 0$ from the Wigner function in saddle-point approximation [31].

C. Classical backpropagation

Classical mechanics has been shown to provide a good and effortless description of the electron dynamics in the continuum (see, e.g., Refs. [32–40]). This is a welcome side effect but the real reason why we use classical dynamics is to be able to identify tunneling dynamics, or more precisely under-barrier motion whose spatial boundaries at a given energy are local properties which can only be defined classically. To reach the barrier, we first will propagate the ionized phase-space distribution $\rho(\boldsymbol{p}, \boldsymbol{r}, t)$ backward in time, starting at time t'. Formally, the time evolution is given by Liouville's equation, which we discretize with the help of classical trajectories. They are propagated solving Newton's equations by means of a fourth-order Runge–Kutta method.

D. The tunneling projector

As already mentioned, the classical description allows for detecting tunneling, or more precisely, to determine the probability that a certain phase-space density tunnels, for which one can consider different criteria. Such criteria apply conditions on phase-space coordinates, in the simplest case to position or momentum. Thereby the dimension of the phase space is reduced.

Formally, the conditions leading to a lower-dimensional phase-space density are most easily introduced by a projection operator Π. It monitors the evolution of ionized phase-space density while being backpropagated and detects, according to criteria which need to be specified, if tunneling occurs at any given time t. It is therefore given as a density in time,

$$\Pi_\xi = \delta(\xi(\boldsymbol{\gamma})) \frac{d\xi}{dt}, \qquad (5a)$$

where $\boldsymbol{\gamma}(t) \equiv \{\boldsymbol{p}(t), \boldsymbol{r}(t)\}$ describes a trajectory which should fulfill $\xi(\boldsymbol{\gamma}(t)) = 0$ to count as a tunneling contribution. By means of the projector Π_ξ one can put various tunneling criteria ξ, that have been adopted in former investigations, side by side. Its abstract definition Eq. (5a) becomes clearer in Secs. III and IV below, where we discuss two essentially different conditions ξ, cf. Eqs. (7) and (11).

Π_ξ is a projector, provided that each trajectory $\boldsymbol{\gamma}(t)$ contributes once at most, i.e., for a unique time. Should $\xi(\boldsymbol{\gamma}(t_j)) = 0$ hold along a trajectory several times, we take the one for which the spatial electron distance is closest to the nucleus $\boldsymbol{\gamma}(t_{\boldsymbol{\gamma}}) \equiv \{\boldsymbol{\gamma}(t_j)| \min_j (r_j)\}$ in line with a tunneling process. Hence, extracting to which tunneling exit time τ an individual trajectory contributes, the projector Eq. (5a), applied to a backpropagated phase-space density, generates the fully

differential tunneling density,

$$\frac{d^{D+1}P_{\text{tun};\xi}}{d\tau\,d\boldsymbol{\gamma}} \equiv \rho_{\text{tun};\xi}(\boldsymbol{\gamma},\tau) = \Pi_\xi\,\rho(\boldsymbol{\gamma},t), \tag{5b}$$

where D is the dimension of $\boldsymbol{\gamma}$, in our case of a planar one-electron problem, $D = 4$. The total tunneling probability is given by

$$P_{\text{tun};\xi} = \int d\tau\,d\boldsymbol{\gamma}\,\rho_{\text{tun};\xi}(\boldsymbol{\gamma},\tau). \tag{5c}$$

Below we will discuss and compare specific choices for ξ, which will elucidate how the tunneling projector works.

E. Nontunneled fraction

With P_{tun} from Eq. (5c) the tunneling projector not only determines the probability for tunneling ionization, it also identifies the fraction χ of electrons which was *not* ionized by tunneling but through another process [9],

$$\chi = \frac{P_{\text{ion}} - P_{\text{tun}}}{P_{\text{ion}}}, \tag{6}$$

where $P_{\text{ion}} = \int |\psi(\boldsymbol{r},t')|^2 d^2 r$ is the total ionization probability with $\psi(\boldsymbol{r},t')$ from Eq. (2). If this nontunneled fraction χ is small, tunneling ionization dominates over other ionization mechanisms, e.g., multiphoton or over-barrier ionization.

III. TUNNELING EXIT BY VELOCITY CONDITION

Earlier we have defined the tunnel exit by a minimal condition [9], namely that the velocity $\boldsymbol{k} \equiv \dot{\boldsymbol{r}} = \boldsymbol{p} + \boldsymbol{A}$ in the instantaneous field direction is zero, which leads to the projector

$$\Pi_p = \delta(\xi_p)\frac{d\xi_p}{dt} \quad \text{with} \quad \xi_p = \boldsymbol{k}\cdot\boldsymbol{F}(t). \tag{7}$$

Here, $\boldsymbol{F}(t)$ is the electric field of the laser. Tunneling is synonymous with classically forbidden dynamics and therefore requires at least one suitably chosen phase-space coordinate to be imaginary throughout the barrier. The tunnel exit is defined as the border between classically forbidden and allowed motion (with real velocities) and since for a continuous potential the velocities will be continuous, we must have a zero for at least one velocity component. Note, that this condition Π_p is independent of the instantaneous energy $E(t)$ of the system, a fact which will turn out to be crucial.

A. Tunneling ionization rate

To put the tunneling criterion, as just defined, into perspective, it is natural to compare the resulting tunneling (exit) time distributions $dP_{\text{tun};p}/d\tau = \int d\boldsymbol{\gamma}\,\rho_{\text{tun};p}(\boldsymbol{\gamma},\tau)$ to the well known instantaneous Ammosov–Delone–Krainov (ADK) rate [41–43], the Perelomov–Popov–Terent'ev (PPT) rate [44–49] and the Yudin–Ivanov (YI) rate [50], whose analytical formula are listed in Appendix A. Although these rates are for electrons in three dimensions, there is good agreement in shape with our calculations in two dimensions, as one can see in Fig. 3. Indeed, the dominant (exponential) dependence of the analytical rates on intensity is independent of dimensionality. Only the prefactor differs, which is reflected by the scaling
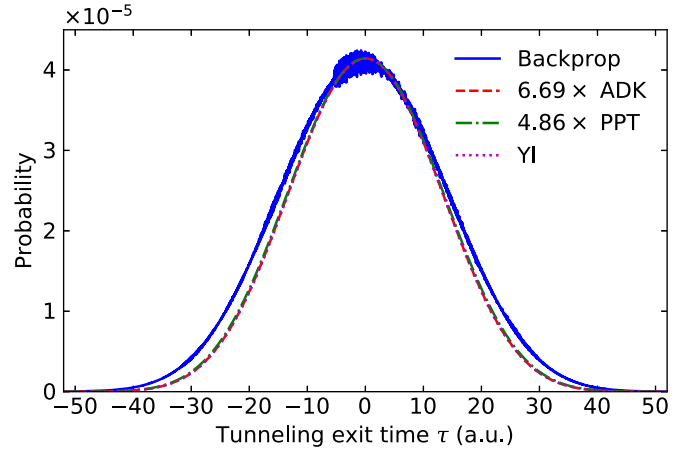

FIG. 3. The distribution of the tunneling exit time (blue solid line) compared to the instantaneous ADK rate (red dashed line), PPT rate (green dash-dotted line), and YI rate (magenta dotted line). The latter three are hardly distinguishable. Laser parameters are the same as in Fig. 2. The rates are scaled to match at maxima.

factors in Fig. 3; for more details see Appendix B. Hence, our tunneling rate obtained by backpropagation may be seen as the first validation of the ADK and PPT theories by a tunneling approach that does not approximate the electron dynamics in the first place.

B. Tunneling and asymptotic momentum distributions

While there is no substantial difference in the tunneling ionization rate obtained by various analytical approximations and the backpropagation as we have seen, it is well known that the momentum distributions of ADK and PPT theories are different. This is a good motivation to take a closer look at the corresponding distributions from backpropagation, in addition to the promise of more detailed understanding of the tunneling dynamics. To this end two distributions of the (kinetic) momentum $k_\perp$, perpendicular to the instantaneous field direction $\boldsymbol{F}(t)/F(t)$ at the tunnel exit, are presented in Fig. 4(a), namely (i) the distribution averaged over the tunneling ionization times (blue solid line) and (ii) the distribution taken at the pulse center $t = 0$ (yellow solid line). These results from backpropagation are contrasted with the ADK (red dashed) and PPT (green dash-dotted) curves.

Obviously and as well known, the ADK description assumes $\langle k_\perp \rangle = 0$ and therefore, the momentum distribution peaks about zero. In contrast, the PPT distribution has finite $\langle k_\perp \rangle$ and is close to the backpropagated results, in shape as well as peak position. Note that at the tunnel exit the two distributions from backpropagation almost agree implying that most of the ionization events contributing to the perpendicular momentum occur close to maximal electric field. Note also that we define $k_\perp > 0$ as pointing opposite to the rotation direction of the laser field vector.

It is instructive to examine how these tunneling exit distributions are reflected in the asymptotic distributions, accessible by experiment and shown in Fig. 4(b). Since ADK as well as PPT assume free electron motion in the laser field, the respective width in momentum space remains unchanged. The
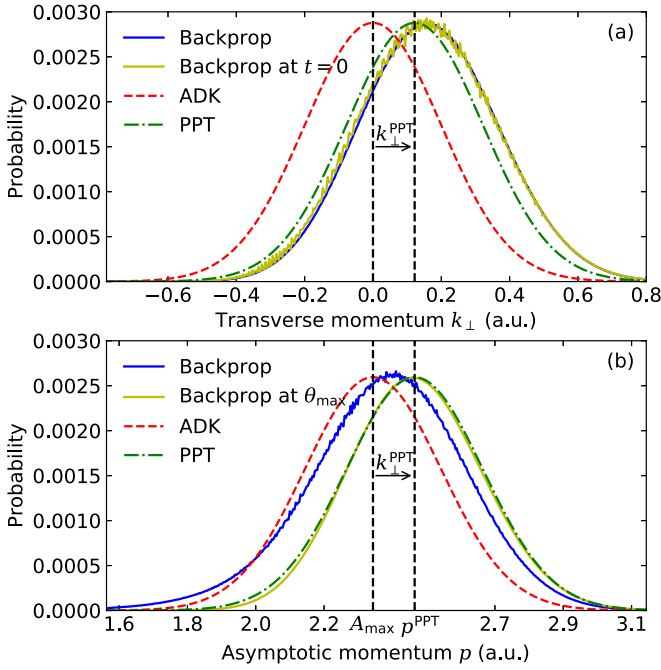
FIG. 4. The distribution of (a) transverse momentum at the tunnel exit (blue solid line: integrated over tunneling exit time; yellow solid line: sliced at pulse center $t = 0$) with $A_x(0) = A_0/\sqrt{1 + \epsilon^2} \equiv A_{\max}$, (b) asymptotic momentum (blue solid line: integrated over emission angle; yellow solid line: sliced at maximal emission angle $\theta_{\max}$). Also shown are the ADK (red dashed line) and PPT distributions (green dash-dotted line) of transverse and asymptotic momentum, scaled to the respective maxima of the distributions from backpropagation. Laser parameters are the same as in Fig. 2. The central momenta of PPT distributions are shifted by $k_\perp^{PPT}$ w.r.t. the ADK distributions, while both asymptotic distributions are shifted by $A_{\max}$ w.r.t. the tunneling exit distributions, all marked by black dashed lines.

asymptotic distributions must peak in the direction of electron propagation, i.e., the radial momentum can be directly deduced from the tunneling exit distributions through the conservation of the canonical momentum: Simply put, the drift momentum at the tunnel exit is converted into asymptotic radial momentum

p. Clearly, the ADK distribution must peak about the drift momentum, i.e., $p^{ADK} = A_0/\sqrt{1 + \epsilon^2} \equiv A_{\max}$ since this was necessary to have zero mean velocity at the tunnel exit. The PPT distribution has at the tunnel exit in perpendicular direction the additional contribution $k_\perp^{PPT}$ [44–49] (see also Ref. [51]), such that asymptotically the central momentum is $p^{PPT} = k_\perp^{PPT} + A_{\max}$, in almost perfect agreement with the backpropagated distribution evaluated at the angle of maximal emission. Averaging over all ionized flux should give a distribution centered at lower momentum since also other emission angles with smaller laser intensities contribute. This is indeed the case, as the solid blue curve in Fig. 4(b) reveals.

From Fig. 4 we may conclude that the PPT theory predicts the asymptotic momentum distribution very well, while the initial transverse momentum is slightly underestimated. Similarly, the initial transverse momentum spread is slightly wider than predicted by ADK and PPT theories, while the asymptotic PPT momentum spread agrees quite well with the numerical distribution. One should keep in mind that both analytical theories neglect the Coulomb field.

The reader is referred to Appendix C for a study on the influence of the initial conditions on the final momentum distribution.

C. Double differential tunneling exit distributions

In the most differential setting, a correlated distribution of the tunneling exit time (τ), position (x and y) and transverse momentum ($k_\perp$) can be obtained from Eq. (5b), which contains all the information regarding the tunneling process. To identify characteristic features more easily, we will discuss two double differential distributions.

From Figs. 5(a) and 5(b) it is clear that the ionization mainly happens around the center of the pulse ($\tau = 0$) with an offset in the central transverse momentum from $k_\perp = 0$. The backpropagated and PPT distribution obviously compare quite well.

In Fig. 5(c) we explore spatial tunneling properties. As one can see, the maximal emission probability (in y direction) coincides with the direction of the maximal ionizing field.
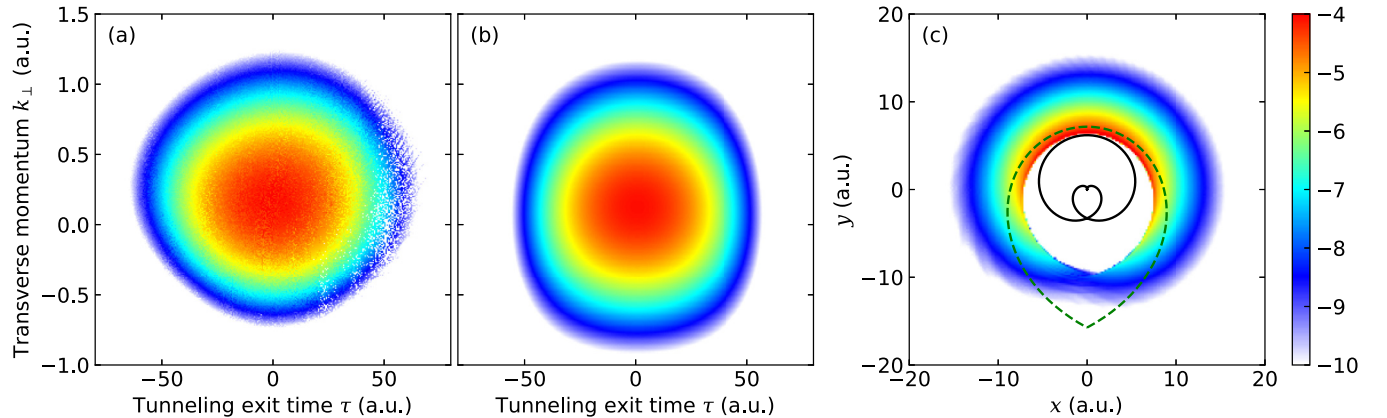

FIG. 5. The correlated distribution of the tunneling exit time and transverse momentum (in logarithmic scale) from backpropagation [panel (a)] and from the analytical PPT theory [panel (b)] with the same scaling factor as in Fig. 3 and the distribution of the tunneling exit position [panel (c)]. Laser parameters are the same as in Fig. 2. The electric field $-\boldsymbol{F}$ (in arb. units) is shown as black solid line and the static tunneling exit as green dashed line in panel (c).
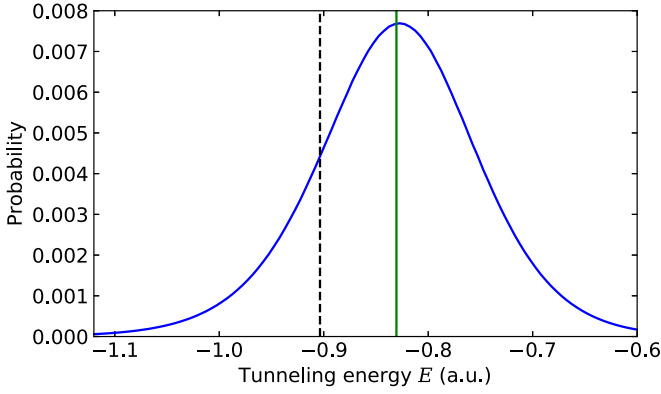
FIG. 6. The distribution of tunneling energy. Laser parameters are the same as in Fig. 2. The green vertical line denotes the mean tunneling energy and the black dashed line denotes the ground-state energy $-I_p$.

However, most ionization occurs *closer* to the parent ion than the static-field tunneling exit position, shown as a green dashed line. This indicates nonadiabaticity [9,52–54], that is, energy is not conserved and in this case the electron absorbs energy during tunneling ionization. Indeed, the tunneling energy distribution (sum of kinetic energy, potential energy, and energy in the field at the tunnel exit) peaks at an energy higher than the ground-state energy as shown in Fig. 6. Consequently, the tunnel exit is closer to the core for the majority of the ionized electrons than assumed in adiabatic tunneling ionization, and the far-out part of the exit corresponds to a tunneling energy lower than the ground-state energy.

D. Intensity dependence of tunneling exit time

So far we have discussed tunneling at a specific intensity to describe its characteristics and how one can formalize them using a quantum-classical approach. In this subsection we discuss the resulting averaged tunneling exit time [see Eqs. (5b) and (7)],

$$\langle \tau \rangle = \int d\tau \, d\boldsymbol{\gamma} \, \tau \, \rho_{\text{tun;p}}(\boldsymbol{\gamma}, \tau), \tag{8}$$

as a function of laser intensity. This is the observable most closely related to the recent debate in the literature [9–17]. As one can see in Fig. 7, $\langle \tau \rangle$ (red dashed line with squares) changes sharply before $2 \times 10^{14} \, \text{W/cm}^2$. From there on, a gradual decrease can be observed. It is a consequence of depletion of the ground state through ionization, getting stronger for increasing intensity. One can correct the exit time for depletion through trajectories that leave the nucleus by tunneling as

$$\langle \tau \rangle_{\text{corr}} = \int d\tau \, \tau \, \frac{\int d\boldsymbol{\gamma} \, \rho_{\text{tun;p}}(\boldsymbol{\gamma}, \tau)}{1 - \int_{-\infty}^{\tau} d\tilde{\tau} \int d\boldsymbol{\gamma} \, \rho_{\text{tun;p}}(\boldsymbol{\gamma}, \tilde{\tau})}. \tag{9}$$

Hence, $\langle \tau \rangle_{\text{corr}}$ (red solid line with squares) remains close to zero until the nontunneled fraction χ of electrons from Eq. (6), shown as a blue solid line with circles, sharply rises. Certainly, we can conclude from there that tunneling ionization implies zero tunneling exit time. But is it also true that zero exit time means tunneling ionization? At a first glance this seems to be the case since in the multiphoton regime at small intensities
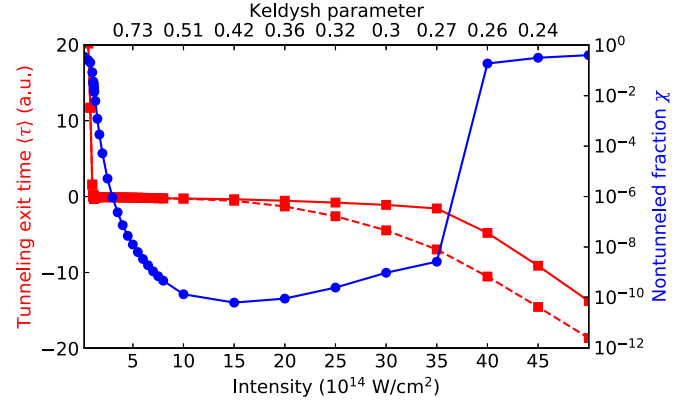

FIG. 7. Intensity dependence of the tunneling exit time (red dashed line) and that corrected for depletion according to Eq. (9) (red solid line). Contributions from over-barrier trajectories fulfilling Eq. (5c) have been excluded; see text. The corresponding nontunneled fraction χ is shown as blue solid line. Laser parameters are the same as in Fig. 2 except for a varying peak intensity.

as well as in the over-barrier regime at large intensities the nontunneled fraction approaches unity.

Yet, in the over-barrier regime, trajectories on their way back may go over the barrier top and reach the nucleus, eventually fulfilling criterion Eq. (7) creating false "tunneling exit" times. However, they circle the nucleus at least once so that they can be easily identified and discarded from P_{tun} in Eq. (5c). There remains for the transition from tunneling to over-barrier-dominated ionization the regime where backpropagated trajectories come close to the top of the barrier and may suffer long time delays or trapping, leading to classically chaotic dynamics. All these trajectories should also count as nontunneled, yet they are not easily identified.

To summarize, while tunneling ionization implies $\langle \tau \rangle \approx 0$, one cannot say that $\langle \tau \rangle \approx 0$ according to criterion Eq. (7) is tantamount to tunneling dynamics.

E. Intensity dependence of the tunneling exit position

Similarly as for $\langle \tau \rangle$, we can construct also for other properties their classical "expectation value" at the tunnel exit with the help of the projector Eq. (7) and the backpropagated ionized electron density. We compare our result for

$$\langle r \rangle = \int d\tau \, d\boldsymbol{\gamma} \, r \, \rho_{\text{tun;p}}(\boldsymbol{\gamma}, \tau) \tag{10a}$$

with

$$\langle r_{\text{exit}} \rangle = \int d\tau \, d\boldsymbol{\gamma} \, r_{\text{exit}}(I_p, F) \, \rho_{\text{tun;p}}(\boldsymbol{\gamma}, \tau) \tag{10b}$$

from different tunneling theories (see Table I) with respective expressions $r_{\text{exit}}(I_p, F)$ for the tunnel exit. Implicitly, these expressions are averaged over the laser pulse through $F = F(t)$ in Eq. (10b). The reason for the consistently larger values $\langle r_{\text{exit}} \rangle > \langle r \rangle$ in Fig. 8 lies in the neglected energy absorption of the electron on the way to the tunnel exit, as already illustrated before. If in Table I the (static) value of the ionization potential I_p is replaced by the actual ionization potential $-E(\tau)$, where $E(\tau)$ is the total energy of the ionizing electron

TABLE I. Different analytical expressions of tunneling exit position r_{exit} from the short-range solution (r_{SFA}), the static field-direction solution (r_{FDM}), the solution in parabolic coordinates (r_{para}) [11,55–57] and the PPT theory (r_{PPT}) [45,47].

r_{exit}	Definition	Remark
r_{SFA}	I_p/F	Coulomb tail neglected
r_{FDM}	$\frac{I_p+\sqrt{I_p^2-4F}}{2F}$	static "field-direction model" [11]
r_{para}	$\frac{I_p+\sqrt{I_p^2-4\beta F}}{2F}$	or "TIPIS" [11], $\beta = 1 - \sqrt{I_p/2}$ [55]
r_{PPT}	$\frac{F}{\omega^2}(\cosh\tau_0 - 1)$	τ_0 is the solution of Eq. (A9)

trajectories at the tunnel exit, then the resulting tunnel exit values $\langle r_{\text{exit}}^{\text{dyn}}\rangle$ become smaller and closer to $\langle r \rangle$, see dashed lines in Fig. 8. Interestingly, the dynamic exit positions of the more sophisticated spatial tunnel exit formulations from PPT and TIPIS are quite close to our $\langle r \rangle$ as can be inferred from Fig. 9(a). This suggests that PPT and TIPIS represent reasonable approximations, provided one knows the instantaneous binding energy $-E(\tau) \neq I_p$ at the tunnel exit.

The nonadiabatic energy gain has also been interpreted and described as a virtual absorption of photons, or polarization of the initial state, followed by a static tunneling ionization [54]. In this study is shown that more photons are virtually absorbed as the Keldysh parameter increases such that the resulting dependence of tunneling energy on laser intensity follows qualitatively the same trend as in Fig. 9(d).

F. Intensity dependence of momentum properties

For completeness we also provide with Figs. 9(b) and 9(c) the intensity dependence for the transverse momentum $k_\perp$ at the tunnel exit and of the asymptotic momentum p respectively, as well as their spread σ. The approximate

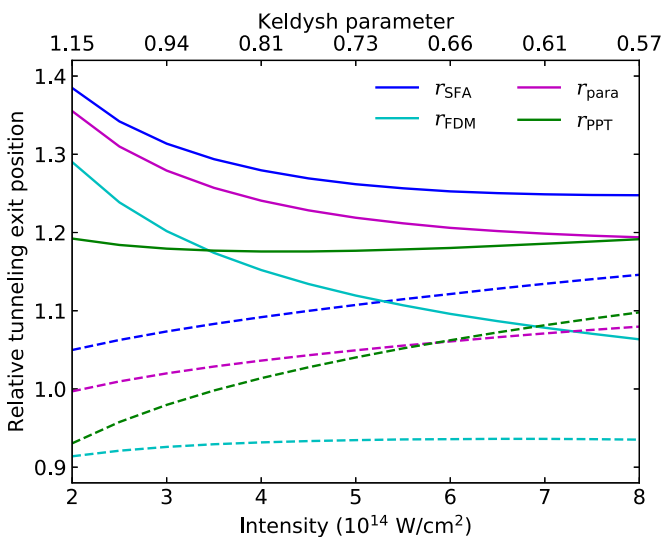
FIG. 8. The intensity dependence of the tunneling exit positions $\langle r_{\text{exit}}\rangle$ according to Eq. (10b) and Table I relative to $\langle r \rangle$ from Eq. (10a), i.e., $\langle r_{\text{exit}}\rangle/\langle r \rangle$, is shown for fixed ionization potential (solid lines) and for dynamic ionization potential (dashed lines). Laser parameters are the same as in Fig. 2 except for a varying peak intensity.

asymptotic momentum closest to our result comes from PPT theory [see green lines in Fig. 9(c)]. This suggests that the laser intensity should be calibrated according to PPT theory instead of ADK theory in the experiment [58,59] at maximal emission angle. Since the momentum spread shows also good agreement, it can be used as well [59]. However, its very weak dependence on the intensity renders this parameter less suitable for intensity calibration than the asymptotic momentum itself.

IV. TUNNELING EXIT BY POSITION CONDITION

In a static tunneling situation, i.e., for a barrier fixed in time, the energy is conserved and the velocity criterion for the tunnel exit as defined in the previous section is used to determine the spatial tunnel exit r_{exit}, such that both criteria are equivalent.

Since (tunneling) ionization by a light pulse is never static, the equivalence of the primary tunneling exit definition (zero velocity) and the spatial tunnel exit (derived with zero velocity by assumption of conserved energy) does not hold, or only in the adiabatic limit of low frequency and long pulses. This is not fulfilled for the attoclock or other attopulse experiments. Therefore, spatial tunnel exits determined under this assumption and tunneling exit times derived from them lead to inconsistent results which, nevertheless, have been widely published. The common ground for comparison has been missing so far, as usually along with a certain tunneling exit criterion also the electron dynamics itself is approximated in a specific way. The classical backpropagation we have introduced offers such a common ground since the ionization dynamics is fully quantum mechanical and does not change for any tunneling criterion.

Therefore, we make the effort to assess the quantitative deviations of the different spatial tunneling criteria among each other, and the consistently formulated velocity criterion for the tunnel exit in the following with classical backpropagation. To this end, we first have to formulate the projector for a spatial tunneling exit criterion r_{exit}, constructed analogously to Eq. (7),

$$\Pi_r = \delta(r - r_{\text{exit}})\frac{dr}{dt}, \qquad (11)$$

where r_{exit} is the tunneling exit position in different models given in Table I.

A. Intensity dependence of tunneling parameters

If $r = r_{\text{exit}}$ is used as the stopping criterion during backpropagation, we obtain the fivefold differential tunneling exit distribution as before as a function of exit time τ and transverse momentum $k_\perp$, but also as a function of longitudinal momentum $k_\parallel$, and, dependent on the exact nature of the spatial stopping criterion as a function of the angle ϑ, relative to the field direction.

In Fig. 10 we show singly differential tunneling exit distributions to be compared to Fig. 9.

1. Tunneling exit time

First, we note that the tunneling exit time [Fig. 10(a)] is no longer zero for all definitions of r_{exit} considered, an observation in line with what is found in Ref. [15]. This is mainly a consequence of the nonadiabaticity of the tunneling process which
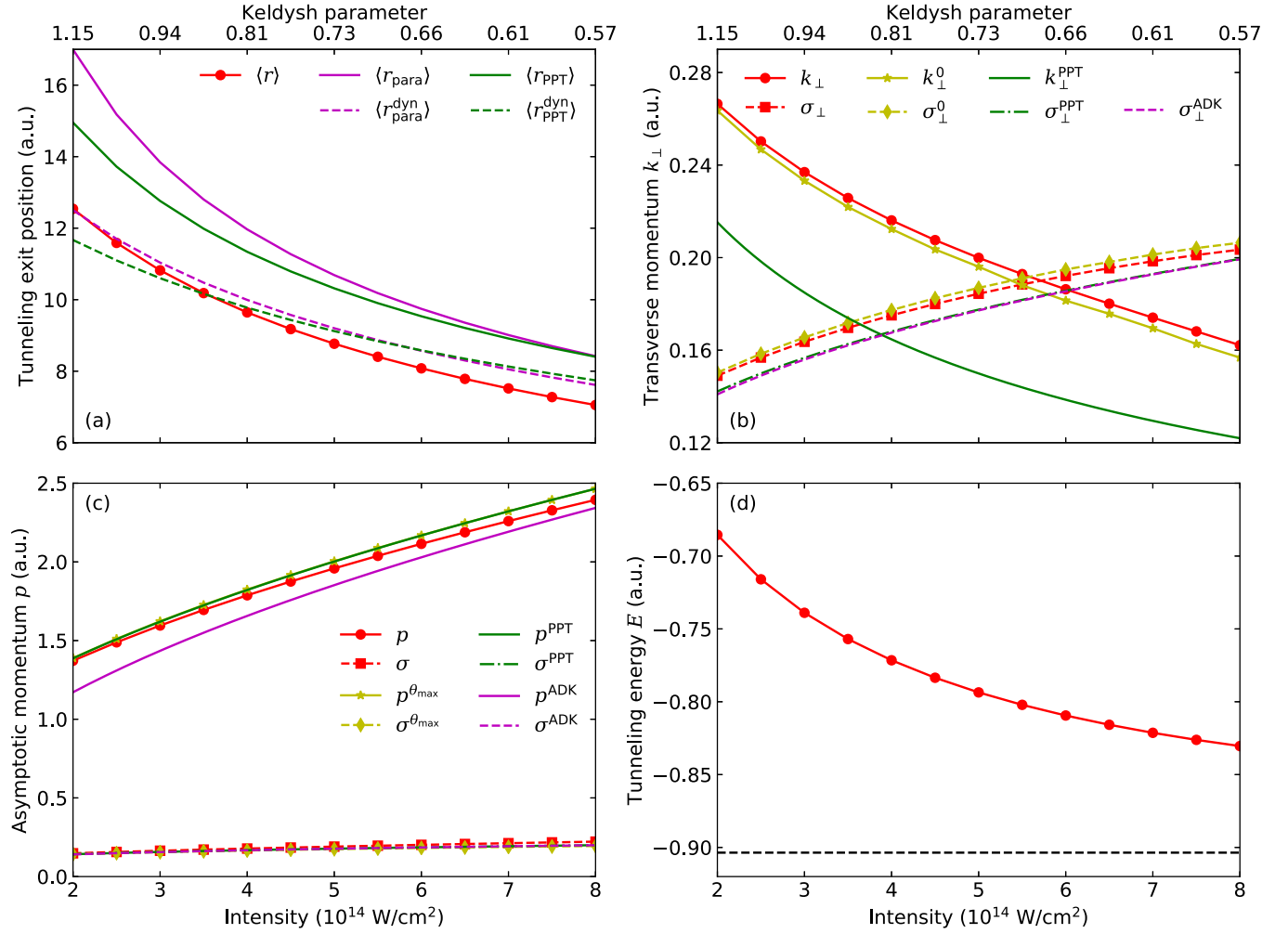
FIG. 9. Comparison between the present backpropagation results (red lines) and various theories for the intensity dependence of the (a) tunneling exit position with line codes and colors as in Fig. 8, (b) transverse tunneling momentum (red lines: integrated over tunneling exit time; yellow lines: sliced at pulse center $t = 0$), (c) asymptotic momentum (red lines: integrated over emission angle; yellow lines: sliced at maximal emission angle $\theta_{\max}$), and (d) full tunneling energy. Further shown in panels (b) and (c) is the transverse momentum from ADK (magenta lines) and PPT (green lines) and in panel (d) the ground-state energy $-I_p$ (black dashed line). Laser parameters are the same as in Fig. 2 except for a varying peak intensity.

moves the tunneling exit position closer to the core [52] than assumed with fixed energy $-I_p$ of the electron. Hence, when a trajectory is stopped prematurely during backpropagation due to adiabatically defined tunneling criteria from I at a larger distance to the core, a positive tunneling time is obtained. However, this nonzero tunneling exit time is a contradiction to the underlying adiabatic assumption, on which the position tunneling criterion is based. It was also (mis)interpreted in the past as a nonzero time delay in the tunneling process (for atoms with single active electron) revealed by the attoclock.

2. Longitudinal momentum

As consequence of the delayed tunneling exit times with respect to the times obtained by the velocity criterion one would expect a finite longitudinal momentum [15,16,58,60–62], since the electron will have been accelerated until the later exit time. The amount of this acceleration and the related longitudinal momentum depend on the specific predefined exit position, cf. Table I. This reasoning is supported by the observation that the

curves of the longitudinal momenta for the different definitions of r_{exit} in Fig. 10(b) exhibit the same order as the curves of the tunneling exit time in Fig. 9(a).

3. Transverse momentum

Similar to the longitudinal momentum, also the transverse momentum in Fig. 10(c) is nonzero with the same order of curves for the different definitions of tunneling exit positions. Only the PPT theory predicts analytically a finite transverse momentum (shown as a green dashed-dotted line), which is for larger intensities close to the one retrieved with the PPT criterion applied to backpropagation.

4. Tunneling exit energy

We can also calculate the mean electron energy at the tunnel exit in Fig. 10(d). This leads to a dramatic inconsistency if in the spatial tunneling exit criteria from Table I, the static energy $-I_p$ is used at the tunnel exit (solid lines) as it is commonly done.
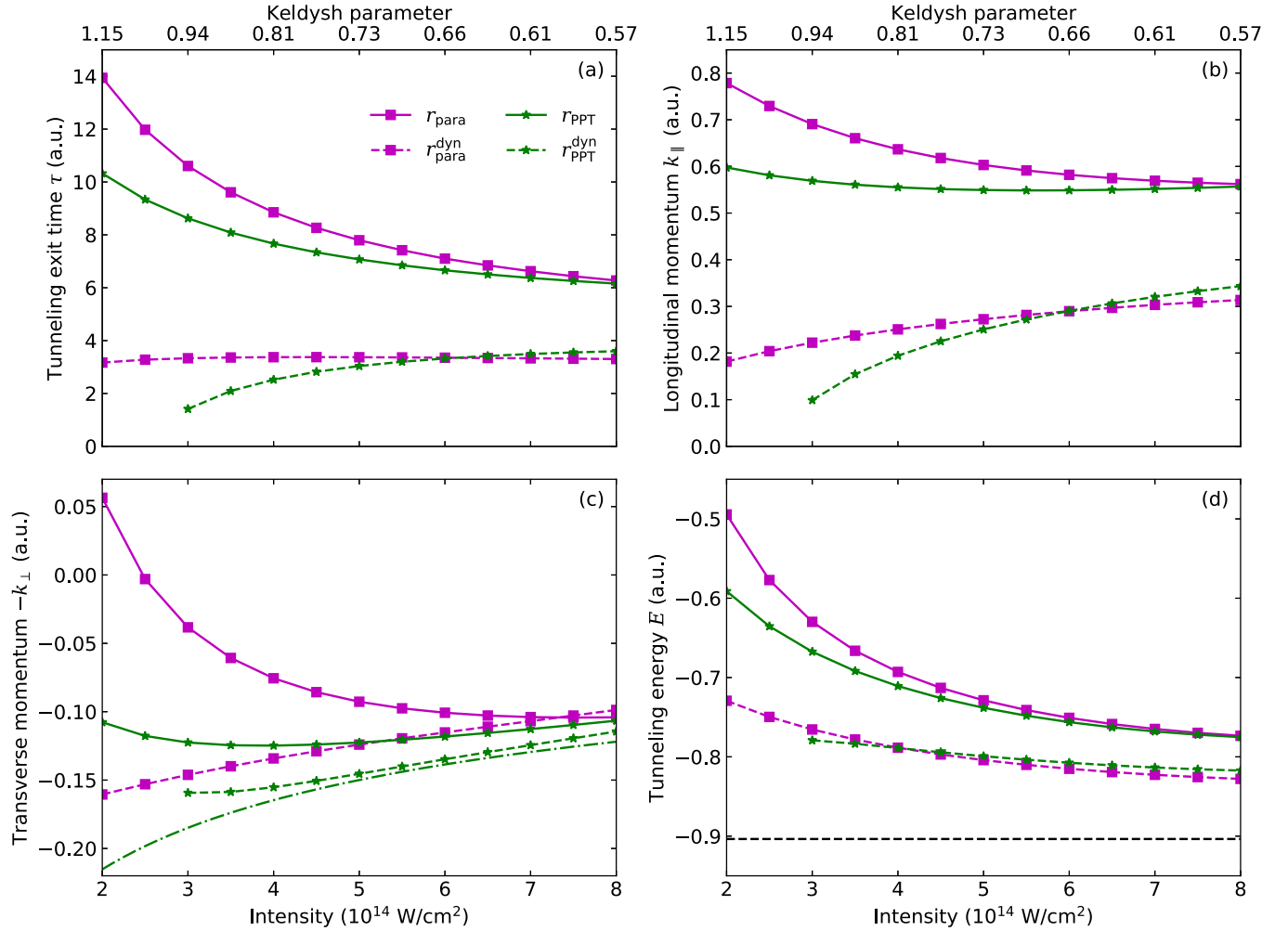
FIG. 10. Intensity dependence of the (a) tunneling exit time, (b) longitudinal tunneling momentum, (c) transverse tunneling momentum, and (d) full tunneling energy, when the position tunneling criterion $r = r_{\text{exit}}$ is used, where r_{exit} is r_{para} (magenta lines with squares) or r_{PPT} (green lines with stars) with static (solid lines) and instantaneous (dashed lines) tunneling energies. Laser parameters are the same as in Fig. 2 except for a varying peak intensity. Further plotted in panel (c) is the analytical PPT transverse momentum (green dash-dotted line) and in panel (d) the ground-state energy $-I_p$ (black dash-dotted line). Note that $r_{\text{PPT}}^{\text{dyn}}$ is so small for $I < 3 \times 10^{14}\,\text{W/cm}^2$ that backpropagated trajectories never reach it.

However, both TIPIS and PPT theories deliver a result (dashed lines) that agrees better with the actual tunneling energy $-E(\tau)$ from Fig. 9(d) if this energy is already used in the respective definition of the spatial tunneling exit criterion instead of the static ionization potential I_p.

B. Failure of the position tunneling criterion

These comparisons clearly show that using a spatial tunneling criterion in a situation of a time-dependent laser field, where one cannot safely assume a fixed binding energy I_p, leads to inconsistencies that render the observables derived with spatial tunneling criteria, in particular the tunneling (exit) time, unreliable.

We finally illustrate this fact with a model, recently used by Teeny *et al.* [15], who found that tunneling exit time and longitudinal momentum is nonzero if the position criterion is used, namely a predefined value r_{exit} derived with a static (maximal) field and ionization potential I_p. However, if

we apply the velocity criterion $k_\parallel = 0$ as discussed in Sec. III to this model, zero tunneling exit time results after correction for depletion, as can be seen in Fig. 11(a).

With the same position tunneling exit criterion, a finite tunneling time was extracted for ionization experiments in argon and krypton [16]. However, if instead the velocity criterion $k_\parallel = 0$ is used, zero tunneling time for argon and krypton in the observed intensity regime results; see Fig. 11(b).

We may conclude that in general knowledge of the electron energy at the tunnel exit is needed for the position tunneling exit criterion (Table I). It is naturally given for static fields by the ionization potential I_p. The latter may be used as an approximation if the laser field changes slowly (adiabatic dynamics). However, the actual energy at the tunnel exit is substantially different from $-I_p$ for few-cycle pulses as was demonstrated in Fig. 9. In this situation, generic for applications of the attoclock, using the static energy I_p to define the tunnel exit leads to inconsistent results. Above all, the position tunneling criterion produces as a consequence of the erroneous use of the
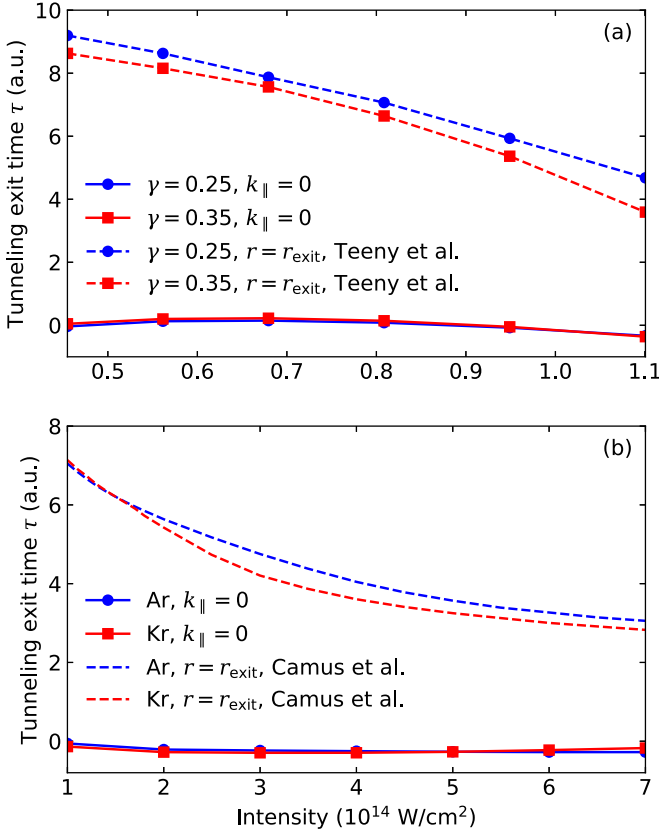
FIG. 11. Intensity dependence of the tunneling exit time obtained by backpropagation using the velocity criterion after correction for depletion (solid lines) compared to Teeny *et al.* [dashed lines, panel (a)] [15] and Camus *et al.* [dashed lines, panel (b)] [16] using position criterion. The same model and laser parameters are used as in Ref. [15] and Ref. [16], respectively.

ionization potential as the energy at the tunnel exit a nonzero tunneling exit time. It was (mis)interpreted in the past as a nonzero time delay in the tunneling process (for atoms with single active electron).

The standard rectification of the (experimental) attoclock angle for the simultaneous interaction of the continuum electron with the laser field and the Coulomb potential suffers from a similar problem: The commonly used trajectory based approaches [10,11,63–65] launch a trajectory from an assumed tunneling exit time and predefined tunneling exit position with certain inferred initial momentum distribution. This procedure carries the inconsistencies just discussed, questioning the validity of the Coulomb correction to the attoclock angle and asking for a better approach to interpret experimental data.

V. MAPPING OFFSET ANGLE TO TUNNELING EXIT TIME

Having established the validity of the velocity tunneling criterion $k_\parallel = 0$, we will construct the correlation between tunneling exit time and offset angle, which provides a link to experimental observables.

To take into account the long-range Coulomb interaction, we obtain the asymptotic momentum $\boldsymbol{p}_0$ using Kepler rules
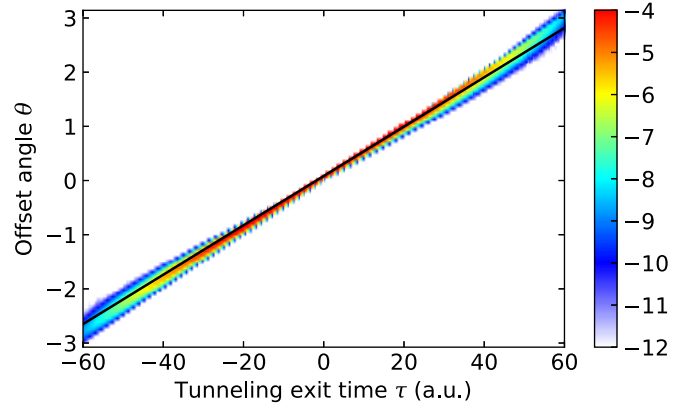

FIG. 12. Correlated distribution of tunneling exit time and offset angle θ (in logarithmic scale). Laser parameters are the same as in Fig. 2. The black solid shows $\theta = \omega(\tau - \tau_{\text{fit}})$.

(although this is accurate only for pure $1/r$ Coulomb potentials) [66]

$$\boldsymbol{p}_0 = p_0 \frac{p_0(\boldsymbol{L} \times \boldsymbol{A}_{\text{RL}}) - \boldsymbol{A}_{\text{RL}}}{1 + p_0^2 L^2}. \tag{12}$$

Here, p_0 is the magnitude of the asymptotic momentum satisfying $\frac{p_0^2}{2} = \frac{p^2}{2} + V(r)$, where $\boldsymbol{r}$ is the position of a particular electron in the final ionized wave packet after the laser pulse, $\boldsymbol{p}$ is its local momentum, $\boldsymbol{L} = \boldsymbol{r} \times \boldsymbol{p}$ is its local angular momentum, and $\boldsymbol{A}_{\text{RL}} = \boldsymbol{p} \times \boldsymbol{L} - \frac{\boldsymbol{r}}{r}$ is the Runge–Lenz vector. The offset angle can be obtained from $\boldsymbol{p}_0$ and the correlated distribution of tunneling exit time versus offset angle is shown in Fig. 12. Evidently, similar to but different from the attoclock, the time axis in Fig. 12 represents not experimentally measured time, but the intrinsic tunneling exit time retrieved by backpropagation. A simple linear regression using fixed slope, i.e., $\tau_{\text{fit}} = \langle\tau\rangle - \langle\theta\rangle/\omega$, with the average taken over the correlated distribution of Fig. 12, reveals directly the tunneling exit time, clear of Coulomb correction:

$$\theta^{\text{fit}}(\tau) = \omega(\tau - \tau_{\text{fit}}). \tag{13}$$

Hence, from the peak offset angle θ_{peak} of an attoclock experiment the tunneling exit time can be determined as $\tau_{\text{peak}} = \theta_{\text{peak}}/\omega + \tau_{\text{fit}}$. The reader is referred to Appendix D for technical details.

Figure 13 provides a comparison of the intensity dependence of the tunneling exit time obtained by such fitting and mapping procedure τ_{peak} and the expected tunneling time $\langle\tau\rangle$ obtained directly (cf. Fig. 7), illustrating that the two methods give very close results. Such good agreement has important implications for future experiments. Once the experimental data is available, a mapping between the data and the tunneling exit time can be created using the backpropagation method (using the velocity tunneling criterion). Hence, the tunneling exit time, free from Coulomb corrections, can be extracted routinely.

VI. CONCLUSION

We have provided a comprehensive study of electron properties at the tunnel exit in the regime of tunneling ionization by circularly polarized light for a planar helium atom with
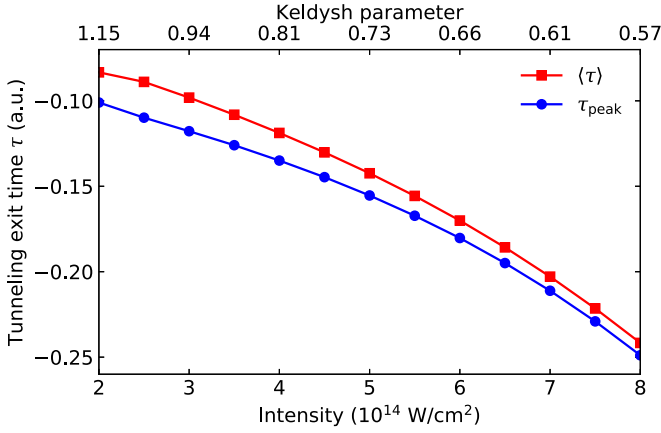
FIG. 13. Intensity dependence of the tunneling exit time with a comparison between the time obtained by fitting and mapping τ_{peak} (blue line with circles) and the expected tunneling exit time $\langle \tau \rangle$ (red line with squares, cf. Fig. 7). Laser parameters are the same as in Fig. 2 except for a varying peak intensity.

a single active electron using classical backpropagation. Our approach employs a fully quantum-mechanical treatment of the tunneling process without *ad hoc* assumptions or approximations. The ionized wave packet is then classically propagated backward in time up to a stopping criterion for the tunnel exit. This backpropagation naturally includes all interactions, it automatically accounts for the Coulomb correction in the attoclock measurements and we can quantify the validity of the tunneling scenario in the first place via the introduction of the so called "nontunneled fraction" of electrons.

The backpropagation method gives highly differential phase-space information regarding tunneling and enables the comparison of different tunneling criteria on the same footing. In the case tunneling is characterized by the velocity criterion $k_{\parallel} = 0$, a correlated distribution of tunneling exit time, position, and transverse tunneling momentum can be obtained. We can draw the following conclusions:

(A) Straightforward projections of this correlated distribution reveals that in the tunneling regime, (i) the tunneling exit time is around zero, (ii) the tunneling exit point is closer to the core than predicted with adiabatic theories, (iii) the tunneling electron has a larger transverse momentum offset and spread than predicted, and (iv) the tunneling energy is above the initial-state energy due to nonadiabatic effects.

(B) While the velocity criterion $k_{\parallel} = 0$ gives zero tunneling exit time, different position criteria $r = r_{\text{exit}}$ give nonzero tunneling exit time, mainly because the nonadiabatic behavior of tunneling dynamics is not taken into account. The nonzero tunneling exit time was (mis)interpreted in the past as a nonzero time delay in the tunneling process for atoms with a single active electron.

(C) In a wider context, this has the important implication that commonly used trajectory based methods (with trajectories starting from an assumed tunneling exit time and predefined tunneling exit position with certain inferred initial momentum distribution to reconstruct the asymptotic momentum distribution) may lead to inaccuracies and inconsistencies. On the other hand, with the backpropagation method using the velocity criterion, we can obtain a correlation between

tunneling exit time and offset angle, which provides a mapping between the experimental observables and the exit time of interest. Such mapping may serve as a convenient tool to extract timing information from future attoclock experiments.

Finally, the present approach has opened the way to use exact quantum propagation to define a tunnel exit in phase space. For the latter, we have on purpose restricted ourselves to purely classical backpropagation, since it can be easily implemented. From a theoretical perspective, this picture is not yet complete since one may resort to complex classical mechanics, which has more flexibility but retains the locality of the dynamics. Locality is convenient to identify tunneling and necessary to define a tunnel exit, which is in the end, always an approximation providing insight into physically relevant processes.

APPENDIX A: ANALYTICAL TUNNELING RATE AND TUNNELING MOMENTUM DISTRIBUTION

We summarize here the instantaneous rate formula starting from the ground s-state exposed to a circularly polarized laser field as we have used in this article. Note that the formula differ for different initial state and laser polarization. The instantaneous (or quasistatic) ADK rate can be written as [41–43]

$$w_{\text{ADK}}(F) = \frac{F D^2}{8 \pi Z} \exp\left(-\frac{2F_0}{3F}\right), \tag{A1}$$

where

$$D = \left(\frac{4 e Z^3}{F n^{*4}}\right)^{n^*}, \tag{A2}$$

$e = 2.718\ldots$ is the Euler number, $n^* = Z(2 I_p)^{-1/2}$ is the effective principal quantum number with Z being the asymptotic charge, and $F_0 = (2 I_p)^{3/2}$ with I_p being the ionization potential. The instantaneous PPT rate is expressed as [44–49]

$$w_{\text{PPT}}(F, \omega) = |C_{n^* l^*}|^2 I_p \left[\frac{2 F_0}{F} C(\gamma)\right]^{2 n^* - 1} C(\gamma) h(\gamma)$$
$$\times \exp\left[-\frac{2 F_0}{3F} g(\gamma)\right], \tag{A3}$$

where

$$|C_{n^* l^*}|^2 = \frac{2^{2 n^*}}{n^* \Gamma(n^* + l^* + 1) \Gamma(n^* - l^*)}, \tag{A4}$$

$$C(\gamma) = \frac{\tau_0}{2\gamma} \exp\left\{\int_0^{\tau_0} d\tau \left[\frac{\gamma}{F(\gamma)} - \frac{1}{\tau_0 - \tau}\right]\right\}, \tag{A5}$$

$$F(\gamma) = \left[(\cosh \tau_0 - \cosh \tau)^2 - \left(\frac{\tau}{\tau_0} \sinh \tau_0 - \sinh \tau\right)^2\right]^{1/2}, \tag{A6}$$

$$h(\gamma) = (1 - t_0) \left[\frac{(1 + \gamma^2)(1 - t_0^2)}{(1 + t_0^2/\gamma^2)(1 + t_0^2 + 2t_0^2/\gamma^2)} \right]^{1/2},$$

$$\text{(A7)}$$

$$da9g(\gamma) = \frac{3t_0}{\gamma^2(1 - t_0^2)} \left[(1 + \gamma^2)\left(1 + \frac{t_0^2}{\gamma^2}\right) \right]^{1/2}, \quad \text{(A8)}$$

$\gamma = \frac{\omega}{F}\sqrt{2I_p}$ is the Keldysh parameter, $l^* = n^* - 1$ is the effective orbital quantum number, and τ_0 and t_0 are determined from the transcendental equations

$$\sinh^2 \tau_0 - \left(\cosh \tau_0 - \frac{\sinh \tau_0}{\tau_0} \right)^2 = \gamma^2, \quad \text{(A9)}$$

$$\tanh\left[\frac{1}{1 - t_0}\left(\frac{t_0^2 + \gamma^2}{1 + \gamma^2} \right)^{1/2} \right] = \left(\frac{t_0^2 + \gamma^2}{1 + \gamma^2} \right)^{1/2}. \quad \text{(A10)}$$

The YI rate (up to exponential accuracy) reads [50]

$$w_{\text{YI}}(F) \sim \exp\left[-\frac{F^2}{\omega^3}\Phi\left(\frac{F_{\max}}{F}\gamma \right) \right], \quad \text{(A11)}$$

$$\Phi(\gamma) = (\gamma^2 + 2)\cosh^{-1}\left(1 + \frac{\gamma^2}{2} \right) - \gamma\sqrt{4 + \gamma^2}. \quad \text{(A12)}$$

The transverse tunneling momentum distribution in both ADK and PPT theories is Gaussian-shaped. In ADK theory [41–43], the transverse tunneling momentum centers at zero with a spread of

$$\sigma_\perp^{\text{ADK}} = \sqrt{\frac{F_{\max}}{2\sqrt{2I_p}}}. \quad \text{(A13)}$$

In PPT theory [44–49], the transverse tunneling momentum centers at

$$k_\perp^{\text{PPT}} = \frac{F_{\max}}{\omega}\left(\frac{\sinh \tau_0}{\tau_0} - 1 \right), \quad \text{(A14)}$$

with a spread of

$$\sigma_\perp^{\text{PPT}} = \sqrt{\frac{\omega}{2\tau_0\left[1 + \left(\frac{\tau_0 - \tanh \tau_0}{\tau_0 \tanh \tau_0} \right)^2 \right]}}. \quad \text{(A15)}$$

APPENDIX B: DIMENSIONALITY DEPENDENCE

The strong nonlinear dynamics of tunneling ionization does not depend on the dimensionality, although the overall magnitude does. Thus, the analytical tunneling rates above, although developed initially for three-dimensional atoms, differ only in the prefactors and the exponential factors stay the same for two-dimensional systems. This also applies to the transverse
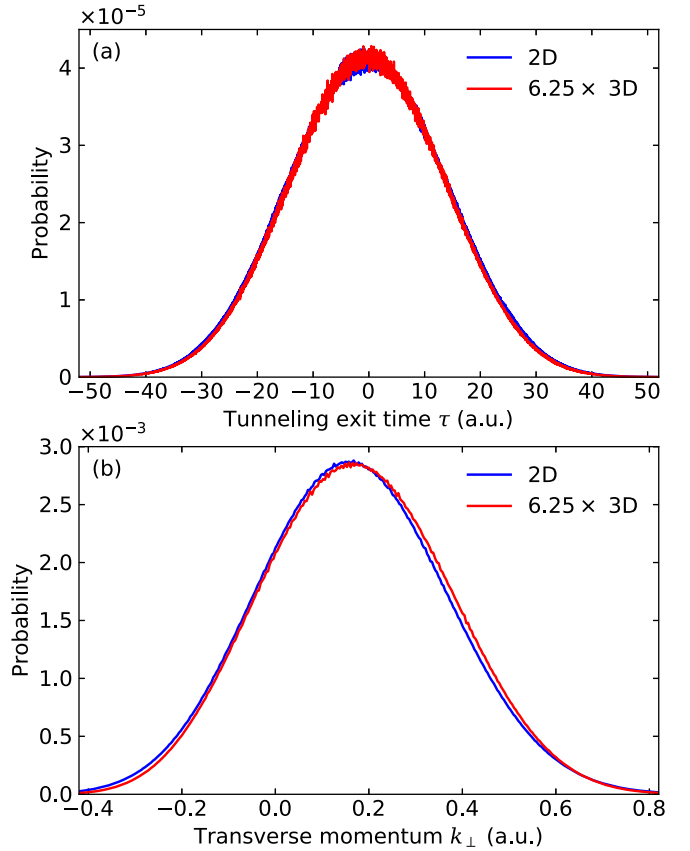

FIG. 14. Comparison of the distributions of (a) tunneling exit time and (b) transverse momentum computed with two-dimensional (2D) and three-dimensional (3D) model helium atom. Laser parameters are the same as in Fig. 2.

momentum shift and spread. Therefore, a comparison of our two-dimensional simulation to the analytical results is possible.

A numerical proof of this dimensionality independence can be seen from, say, a comparison of the distributions of tunneling exit time and transverse momentum in two- and three-dimensional simulations obtained by back-propagation (with velocity tunneling criterion), as shown in Fig. 14.

APPENDIX C: INFLUENCE OF THE INITIAL CONDITIONS ON THE FINAL MOMENTUM DISTRIBUTION

We show in Fig. 15 the final momentum distribution from trajectory based Monte Carlo simulations [10,11,63–65] when the initial conditions are chosen as $r_{\text{exit}} = r_{\text{para}}$ and $k_\perp = k_\perp^{\text{ADK}}$ [panel (a)] and $r_{\text{exit}} = r_{\text{PPT}}$ and $k_\perp = k_\perp^{\text{PPT}}$ [panel (b)] with an assumption of instantaneous response to the laser field. Note that the ADK and PPT tunneling rates are scaled such that they have the same total ionization probability as the quantum-mechanical result as shown in Fig. 2(a).

As it is evident from the figure, both initial conditions give visually similar momentum distributions to Fig. 2(a) and main features of the quantum distribution
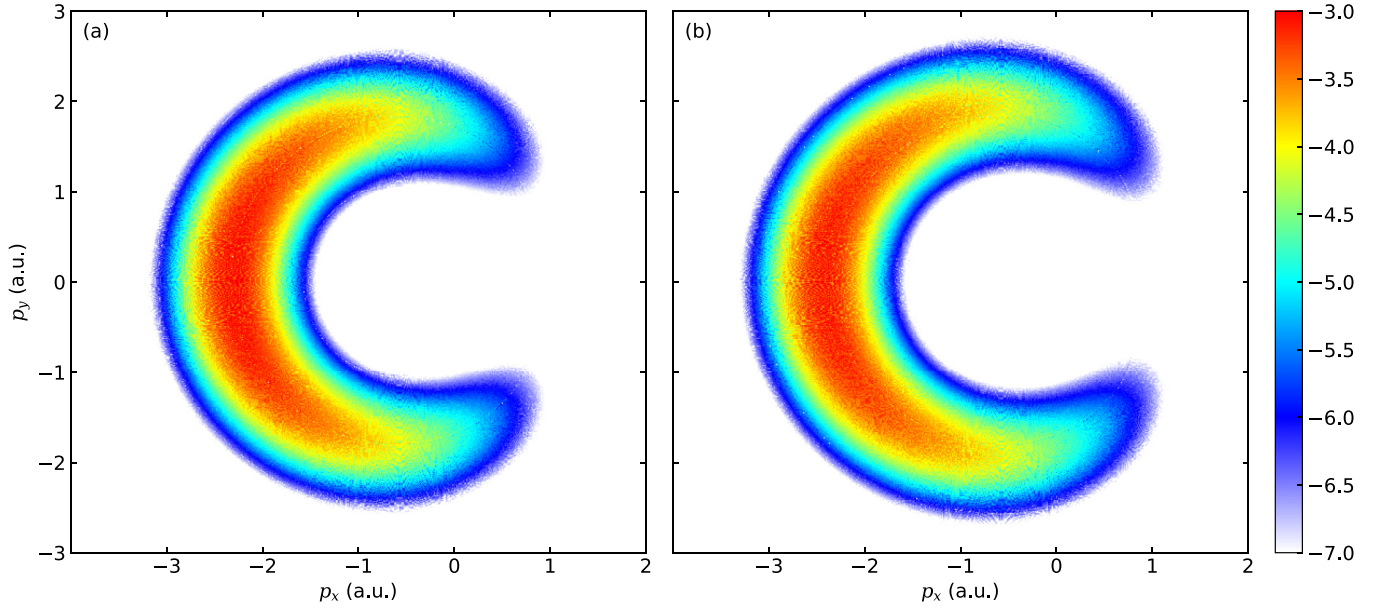
FIG. 15. Momentum distribution obtained from trajectory based Monte Carlo simulations (in logarithmic scale) when the initial conditions are chosen as $r_{\text{exit}} = r_{\text{para}}$ and $k_\perp = k_\perp^{\text{ADK}}$ [panel (a)] and $r_{\text{exit}} = r_{\text{PPT}}$ and $k_\perp = k_\perp^{\text{PPT}}$ [panel (b)]. Laser parameters are the same as in Fig. 2.

are retained. Such similarity can be quantified via the overlap

$$\frac{\int d^2 p \, |\widetilde{\psi}(\boldsymbol{p},t')| \sqrt{\rho_{\text{para}}(\boldsymbol{p},t')}}{\int d^2 p \, |\widetilde{\psi}(\boldsymbol{p},t')|^2} = 0.912, \tag{C1}$$

$$\frac{\int d^2 p \, |\widetilde{\psi}(\boldsymbol{p},t')| \sqrt{\rho_{\text{PPT}}(\boldsymbol{p},t')}}{\int d^2 p \, |\widetilde{\psi}(\boldsymbol{p},t')|^2} = 0.982. \tag{C2}$$

This overlap indicates that, although the initial conditions used by common trajectory based methods [10,11,63–65] are very different (and imprecise) from that extracted by the backpropagation method, the momentum distribution reconstructed is still in reasonably good agreement with quantum results. This suggests, to extract timing information from the attoclock observables, the much more precise backpropagation method (in terms of the mapping technique) is necessary since the attoclock offset angle is not sensitive to tiny changes in the initial conditions. The overlap as shown in Eqs. (4a), (C1), and (C2) may serve as a quantification of the precision of the method used, and it is easy to conclude that the backpropagation method, which guarantees to obtain a momentum distribution as in Fig. 2(b) starting from the tunneling exit parameters

retrieved (up to an error at the level of the nontunneled fraction χ as shown in Fig. 7), is much more precise.

APPENDIX D: WEIGHTED LINEAR REGRESSION FITTING

We detail here the weighted linear regression fitting we have used for the mapping technique to link the experimental observable offset angle to tunneling exit time in Sec. V.

For a correlated distribution $P(\tau,\theta)$ shown in Fig. 12, we seek the optimal fitting parameter τ_{fit} in $\omega(\tau - \tau_{\text{fit}})$ as in Eq. (13), so that

$$f(\tau_{\text{fit}}) = \int d\tau d\theta \, P(\tau,\theta)[\theta - \omega(\tau - \tau_{\text{fit}})]^2 \tag{D1}$$

is minimized. To this end, we require $\frac{\partial f(\tau_{\text{fit}})}{\partial \tau_{\text{fit}}} = 0$, i.e.,

$$\int d\tau d\theta \, P(\tau,\theta)[\theta - \omega(\tau - \tau_{\text{fit}})] = 0, \tag{D2}$$

from which obviously follows

$$\tau_{\text{fit}} = \frac{\int d\tau d\theta \, P(\tau,\theta)\tau}{\int d\tau d\theta \, P(\tau,\theta)} - \frac{\int d\tau d\theta \, P(\tau,\theta)\theta}{\omega \int d\tau d\theta \, P(\tau,\theta)}. \tag{D3}$$

[1] L. A. MacColl, Phys. Rev. **40**, 621 (1932).

[2] R. Landauer and T. Martin, Rev. Mod. Phys. **66**, 217 (1994).

[3] A. S. Landsman and U. Keller, Phys. Rep. **547**, 1 (2015).

[4] S. L. Chin, *From Multiphoton to Tunnel Ionization*, Book Series: Advances in Multi-Photon Processes and Spectroscopy, Vol. 16 (World Scientific, Singapore, 2004), p. 249.

[5] P. Agostini and L. F. DiMauro, *Atomic and Molecular Ionization Dynamics in Strong Laser Fields: From Optical to X-rays*, Book Series: Advances in Atomic, Molecular, and Optical Physics Vol. 61 (Elsevier, Chennai, 2012), p. 117.

[6] S. V. Popruzhenko, J. Phys. B **47**, 204001 (2014).

[7] C. M. Maharjan, A. S. Alnaser, X. M. Tong, B. Ulrich, P. Ranitovic, S. Ghimire, Z. Chang, I. V. Litvinyuk, and C. L. Cocke, Phys. Rev. A **72**, 041403(R) (2005).

[8] P. Eckle, M. Smolarski, P. Schlup, J. Biegert, A. Staudte, M. Schöffler, H. G. Muller, R. Dörner, and U. Keller, Nat. Phys. **4**, 565 (2008).

[9] H. Ni, U. Saalmann, and J. M. Rost, Phys. Rev. Lett. **117**, 023002 (2016).

[10] P. Eckle, A. N. Pfeiffer, C. Cirelli, A. Staudte, R. Dörner, H. G. Muller, M. Büttiker, and U. Keller, Science **322**, 1525 (2008).

[11] A. N. Pfeiffer, C. Cirelli, M. Smolarski, D. Dimitrovski, M. Abu-samha, L. B. Madsen, and U. Keller, Nat. Phys. **8**, 76 (2012).

[12] A. S. Landsman, M. Weger, J. Maurer, R. Boge, A. Ludwig, S. Heuser, C. Cirelli, L. Gallmann, and U. Keller, Optica **1**, 343 (2014).

[13] A. S. Landsman and U. Keller, J. Phys. B **47**, 204024 (2014).

[14] L. Torlina, F. Morales, J. Kaushal, I. A. Ivanov, A. Kheifets, A. Zielinski, A. Scrinzi, H. G. Muller, S. Sukiasyan, M. Y. Ivanov, and O. Smirnova, Nat. Phys. **11**, 503 (2015).

[15] N. Teeny, E. Yakaboylu, H. Bauke, and C. H. Keitel, Phys. Rev. Lett. **116**, 063003 (2016).

[16] N. Camus, E. Yakaboylu, L. Fechner, M. Klaiber, M. Laux, Y. Mi, K. Z. Hatsagortsyan, T. Pfeifer, C. H. Keitel, and R. Moshammer, Phys. Rev. Lett. **119**, 023201 (2017).

[17] U. S. Sainadh, H. Xu, X. Wang, Atia-Tul-Noor, W. C. Wallace, N. Douguet, A. W. Bray, I. A. Ivanov, K. Bartschat, A. S. Kheifets, R. T. Sang, and I. V. Litvinyuk, arXiv:1707.05445.

[18] B. Feuerstein and U. Thumm, J. Phys. B **36**, 707 (2003).

[19] X. Wang, J. Tian, and J. H. Eberly, Phys. Rev. Lett. **110**, 243001 (2013).

[20] C. Møller, D. Kgl. Danske Vidensk. Selsk. Mat.-Fys. Medd. **23**(1), 1 (1945).

[21] T. Gorin, T. Prosen, T. H. Seligman, and M. Žnidarič, Phys. Rep. **435**, 33 (2006).

[22] A. Peres, Phys. Rev. A **30**, 1610 (1984).

[23] J. Vaníček and E. J. Heller, Phys. Rev. E **68**, 056208 (2003).

[24] J. Werschnik and E. K. U. Gross, J. Phys. B **40**, R175 (2007).

[25] C. Brif, R. Chakrabarti, and H. Rabitz, New J. Phys. **12**, 075008 (2010).

[26] E. P. Wigner, Phys. Rev. **98**, 145 (1955).

[27] F. T. Smith, Phys. Rev. **118**, 349 (1960).

[28] J. Su, H. Ni, A. Becker, and A. Jaroń-Becker, Phys. Rev. A **87**, 033420 (2013).

[29] J. Su, H. Ni, A. Becker, and A. Jaroń-Becker, J. Mod. Opt. **60**, 1484 (2013).

[30] X. M. Tong and C. D. Lin, J. Phys. B **38**, 2593 (2005).

[31] S. Jin and X. Li, Physica D **182**, 46 (2003).

[32] J. M. Rost, Phys. Rep. **297**, 271 (1998).

[33] K. I. Dimitriou, D. G. Arbó, S. Yoshida, E. Persson, and J. Burgdörfer, Phys. Rev. A **70**, 061401(R) (2004).

[34] S. Chelkowski and A. D. Bandrauk, Phys. Rev. A **71**, 053815 (2005).

[35] X. Y. Lai, Q. Y. Cai, and M. S. Zhan, New J. Phys. **11**, 113035 (2009).

[36] S. Nagele, R. Pazourek, J. Feist, K. Doblhoff-Dier, C. Lemell, K. Tőkési, and J. Burgdörfer, J. Phys. B **44**, 081001 (2011).

[37] A. Kästner, U. Saalmann, and J. M. Rost, Phys. Rev. Lett. **108**, 033201 (2012).

[38] F. Mauger, A. D. Bandrauk, A. Kamor, T. Uzer, and C. Chandre, J. Phys. B **47**, 041001 (2014).

[39] K. Zhang, Y. H. Lai, E. Diesen, B. E. Schmidt, C. I. Blaga, J. Xu, T. T. Gorman, F. Légaré, U. Saalmann, P. Agostini, J. M. Rost, and L. F. Di Mauro, Phys. Rev. A **93**, 021403(R) (2016).

[40] J. S. Briggs and J. M. Feagin, New J. Phys. **18**, 033028 (2016).

[41] M. V. Ammosov, N. B. Delone, and V. P. Krainov, Sov. Phys. JETP **64**, 1191 (1986).

[42] N. B. Delone and V. P. Krainov, Phys. Usp. **41**, 469 (1998).

[43] M. Y. Ivanov, M. Spanner, and O. Smirnova, J. Mod. Opt. **52**, 165 (2005).

[44] A. M. Perelomov, V. S. Popov, and M. V. Terent'ev, Sov. Phys. JETP **23**, 924 (1966).

[45] A. M. Perelomov, V. S. Popov, and M. V. Terent'ev, Sov. Phys. JETP **24**, 207 (1967).

[46] A. M. Perelomov and V. S. Popov, Sov. Phys. JETP **25**, 336 (1967).

[47] V. D. Mur, S. V. Popruzhenko, and V. S. Popov, J. Exp. Theor. Phys. **92**, 777 (2001).

[48] V. S. Popov, Phys. Usp. **47**, 855 (2004).

[49] B. M. Karnakov, V. D. Mur, S. V. Popruzhenko, and V. S. Popov, Phys. Usp. **58**, 3 (2015).

[50] G. L. Yudin and M. Y. Ivanov, Phys. Rev. A **64**, 013409 (2001).

[51] J. Kaushal and O. Smirnova, Phys. Rev. A **88**, 013421 (2013).

[52] M. Klaiber, K. Z. Hatsagortsyan, and C. H. Keitel, Phys. Rev. Lett. **114**, 083001 (2015).

[53] E. E. Serebryannikov and A. M. Zheltikov, Phys. Rev. Lett. **116**, 123901 (2016).

[54] M. Klaiber and J. S. Briggs, Phys. Rev. A **94**, 053405 (2016).

[55] C. Z. Bisgaard and L. B. Madsen, Am. J. Phys. **72**, 249 (2004).

[56] B. Hu, J. Liu, and S. G. Chen, Phys. Lett. A **236**, 533 (1997).

[57] C. Hofmann, A. S. Landsman, C. Cirelli, A. N. Pfeiffer, and U. Keller, J. Phys. B **46**, 125601 (2013).

[58] J. W. Geng, L. Qin, M. Li, W. H. Xiong, Y. Liu, Q. Gong, and L. Y. Peng, J. Phys. B **47**, 204027 (2014).

[59] C. Hofmann, T. Zimmermann, A. Zielinski, and A. S. Landsman, New J. Phys. **18**, 043011 (2016).

[60] M. Li, J. W. Geng, M. Han, M. M. Liu, L. Y. Peng, Q. Gong, and Y. Liu, Phys. Rev. A **93**, 013402 (2016).

[61] M. Han, M. Li, M. M. Liu, and Y. Liu, Phys. Rev. A **95**, 023406 (2017).

[62] J. Tian, X. Wang, and J. H. Eberly, Phys. Rev. Lett. **118**, 213201 (2017).

[63] M. Li, J. W. Geng, H. Liu, Y. Deng, C. Wu, L. Y. Peng, Q. Gong, and Y. Liu, Phys. Rev. Lett. **112**, 113002 (2014).

[64] X. Song, C. Lin, Z. Sheng, P. Liu, Z. Chen, W. Yang, S. Hu, C. D. Lin, and J. Chen, Sci. Rep. **6**, 28392 (2016).

[65] N. I. Shvetsov-Shilovski, M. Lein, L. B. Madsen, E. Räsänen, C. Lemell, J. Burgdörfer, D. G. Arbó, and K. Tőkési, Phys. Rev. A **94**, 013415 (2016).

[66] N. I. Shvetsov-Shilovski, D. Dimitrovski, and L. B. Madsen, Phys. Rev. A **85**, 023428 (2012).